International Journal of Plasticity 125 (2020) 80–96

Contents lists available at ScienceDirect

International Journal of Plasticity

journal homepage: http://www.elsevier.com/locate/ijplas

Ductile fracture of dual-phase steel sheets under bending

Yu Liu [a], Dongwei Fan [b], Shrikant P. Bhat [b], Ankit Srivastava [a,*]

[a] Department of Materials Science and Engineering, Texas A&M University, College Station, TX, USA
[b] ArcelorMittal Global R&D, East Chicago, East Chicago, IN, USA

ARTICLE INFO

Keywords:
Fracture
Microstructures
Metallic material
Finite elements
Bendability

ABSTRACT

Ductile fracture involving nucleation, growth and coalescence of microscale voids limits the performance, safety, reliability and manufacturability of a variety of metallic components and structures. This phenomenon is affected by length-scales induced by the geometry of deformation, loading conditions and microstructure of the material. For example, under uniaxial tension, dual-phase (DP) advanced high strength steel sheets exhibit similar flow response along rolling (RD) and transverse directions (TD) with ductility along RD being either equal to or greater than TD. However, the bendability of sheet specimens with bend axis parallel to RD is less than the bendability of sheet specimens with bend axis parallel to TD. The objective of this work is to model the interplay of length-scales induced by bending and microstructure on ductile fracture of DP steel sheets. To this end, microstructure-based finite element calculations of ductile fracture in DP steel sheets under bending have been carried out. In the calculations, DP microstructures in a bend specimen are discretely modeled. Our results show that the microscopic state of stress/strain, and hence, damage evolution in DP steel sheets under bending are highly heterogeneous. The extent to which length-scales induced by bending and DP microstructure affects crack nucleation and early stage crack growth is discussed. Parametric studies to quantify the effect of initial porosity, susceptibility to secondary void nucleation and energy dissipated in damage evolution prior to crack nucleation on the bendability of DP steel sheets have also been carried out.

1. Introduction

The performance, safety, reliability and manufacturability of a variety of metallic components and structures are limited by ductile fracture. At room temperature, ductile fracture of engineering metals and alloys involves nucleation, growth and coalescence of microscale voids (Benzerga et al., 2016). This phenomenon is affected by the interlacing of length-scales induced by geometry of deformation, loading conditions and/or heterogeneous microstructure of the material. These length-scales in turn interact and evolve. For instance, local heterogeneous deformation fields can produce substantial microstructural modifications resulting in often unknown and counterintuitive subsequent fracture process. The objective of this work is to model the effect of length-scales induced by geometry of deformation, in particular bending, and material microstructure on ductile fracture of dual-phase (DP) advanced high strength steel (AHSS) sheets.

DP steel sheets with yield and tensile strengths in excess of 300*MPa* and 600*MPa*, respectively, are one of the most widely sought after AHSS for automotive applications (Kuziak et al., 2008) where safety, vehicle weight reduction and emission reduction are of

* Corresponding author.
E-mail address: ankit.sri@tamu.edu (A. Srivastava).

https://doi.org/10.1016/j.ijplas.2019.08.019
Received 16 May 2019; Received in revised form 14 August 2019; Accepted 25 August 2019
Available online 29 August 2019

paramount importance (Bhattacharya, 2011; Joost, 2012). DP steels were introduced in mid-1970s (Rashid, 1981) and since then have experienced the fastest growth in automotive industry (Bhattacharya, 2011). These are produced on continuous annealing lines that allow intercritical heating into the ferrite-austenite phase field followed by rapid cooling to cause diffusionless austenite to martensite transformation (Rashid, 1981). The final microstructure of DP steels primarily consists of hard martensite islands dispersed in a soft ferrite phase matrix. The presence of two elastic-plastic phases with contrasting strength and strain hardenability gives rise to complex deformation behavior, especially for DP steels with high martensite content and tensile strength of order $1GPa$.

While the influence of microstructure on deformation and fracture behavior of DP steel sheets under tensile loading conditions have been a topic of numerous experimental or computational studies, for example, (Davies, 1978; Ramos et al., 1979; Rashid, 1981; Steinbrunner et al., 1988; Choi et al., 2009, 2013; Avramovic-Cingara et al., 2009a, b; Sun et al., 2009a, b; Kadkhodapour et al., 2011; Sodjit and Uthaisangsuk, 2012; Yerra et al., 2013; Chen et al., 2014; Roth and Mohr, 2014; Tasan et al., 2014, 2015; Matsuno et al., 2015; Lai et al., 2015; Marcadet and Mohr, 2015; Alaie et al., 2015; Zhou et al., 2015; De Geus et al., 2015, 2016, 2017; Lai et al., 2016; Gerbig et al., 2018), the role of DP microstructure on complex loading conditions have received far less attention (Embury and Duncan, 1982; Hasegawa et al., 2004; Uthaisangsuk et al., 2009a; Srivastava et al., 2016; Huang et al., 2016). The studies on the microstructural influence on deformation and fracture behavior of DP steels under simplified loading conditions, however, have provided several insights. The tensile stress-strain curve for DP steels with high martensite content has been found to exhibit three characteristic stages (Srivastava et al., 2016). At low stresses, the response is elastic and with increasing stress levels the DP microstructure first reaches yield in the ferrite phase. Following initial yield, a period of steep strain-hardening is observed. In this regime, the martensite remains elastic while ferrite contributes 100% of the plastic strain. This stage continues until martensite reaches yield. At this point, there is a significant reduction in the strain-hardening rate, and both ferrite and martensite continue to deform plastically. The studies pertaining to damage nucleation and evolution in the DP microstructure suggest that volume fraction, morphology and distribution of martensite, and the contrast between the properties of ferrite and martensite phases have a significant influence on damage accumulation. The state-of-the-art also suggests that the damage (or void) nucleation in DP steels occurs by mechanisms such as, decohesion at ferrite/martensite interface, separation of adjacent martensite particles, and/or separation of fractured martensite particles.

The primary benefit of using DP AHSS in automotive body and structural parts is to enhance vehicles' crash resistance while reducing its overall weight. Steels are not inherently light weight material but vehicle weight reduction can be achieved by using AHSS with high density-normalized strength. DP steels with tensile strength of order $1GPa$ and above are one of the targeted structural material for such applications. However, as the strength of DP steel increases, the steel becomes less formable and more prone to fracture under bending dominated manufacturing processes at room temperature (Sriram et al., 2003). In addition, DP steel sheets exhibit contrasting fracture anisotropy along rolling and transverse directions (RD and TD) of the sheet under uniaxial tensile loading versus bending. Under uniaxial tension, DP steel sheets exhibit very similar stress-strain response along RD and TD up to the ultimate tensile strength with ductility along RD being either equal to or greater than ductility along TD (Avramovic-Cingara et al., 2009a; Chen et al., 2014). But under bending, the bendability of sheet specimens with bend axis parallel to RD is less than the bendability of sheet specimens with bend axis parallel to TD (Leu, 1997). This clearly shows that there is a difference between the characterization of fracture in an imposed deformation field that is more or less uniform and the characterization of fracture in a heterogeneous field such as those observed in bending. In the former, a continuum description of fracture, can in principle be based on unstructured material parameters such as strength, strain hardening exponent, and volume fraction of the phases. On the other hand, in the latter, the fracture characterization must involve the interaction of length-scales induced by bending and DP microstructure.

Several attempts have been directed towards modeling ductile fracture of DP steels. These approaches can be divided in to two categories: phenomenological fracture modeling (Bao and Wierzbicki, 2004; Luo and Wierzbicki, 2010; Roth and Mohr, 2014; Marcadet and Mohr, 2015; Andrade et al., 2016) and microstructure-based fracture modeling (Sun et al., 2009a, b; Choi et al., 2009; Uthaisangsuk et al., 2009b, 2011; Kadkhodapour et al., 2011; Paul, 2012; Vajragupta et al., 2012; Perzyński et al., 2014; Matsuno et al., 2015; De Geus et al., 2015, 2016, 2017; Ayatollahi et al., 2016; Gerbig et al., 2018). In phenomenological fracture models, a damage evolution equation is directly fit to macroscopic experimental data without a direct microstructure-fracture correlation. On the other hand, microstructure-based fracture modeling have been largely focused on 2D or 3D representative volume elements of DP microstructures under idealized periodic boundary conditions. No effort has been made to model ductile fracture in DP steels under more realistic loading conditions in order to understand the interaction of length-scales originating from geometry/loading conditions, and material microstructure. Modeling fracture of DP steels under realistic boundary conditions is especially challenging because a loss of stress carrying capacity in the reinforcing phase due to void nucleation greatly affects the overall strain hardening response of the material. This leads to a breakdown in scale separation (Pineau et al., 2016), making it very challenging to mathematically represent the material by an "effective homogenized media."

Here, we carry out microstructure-based finite element modeling to understand the influence of material microstructure on ductile crack nucleation and early stage ductile crack growth in DP steel sheets subjected to 90° V-bend loading conditions. In the calculations, we discretely model the microstructural features, ferrite and martensite phases, of the DP steel in a small area (but large enough to capture nucleation and coalescence of micro-cracks) near the free surface of a thin slice of the bend specimen normal to the bend axis. Both ferrite and martensite phases are modeled using a constitutive relation for progressively cavitating elastic-viscoplastic solid. For the microstructure-based modeling, several 2D SEM (Scanning Electron Microscope) images taken from RD and TD cross-sections of an industrially produced galvannealed DP1000 steel sheet are first digitized. The digitized microstructure is then superimposed on the finite element grid and respective material properties are assigned based on integration points rather than finite elements as in (Srivastava et al., 2014; Osovski et al., 2015b). This allows us to smoothly resolve the interphase boundaries without any numerical complexities. The discretely modeled microstructural features induce microstructural length-scale(s) in finite element calculations (Srivastava et al., 2014, 2017; Osovski et al., 2015b, a; Liu et al., 2019). The effect of length-scales induced by the geometry of

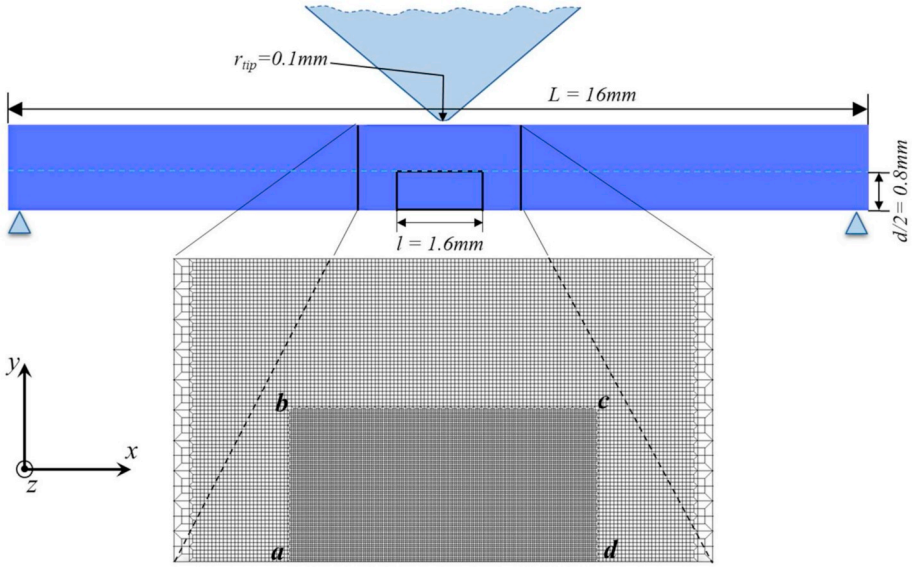

Fig. 1. (top) A schematic of the bend specimen together with imposed constraint and loading conditions. (bottom) A zoomed view of the finite element mesh near the free surface of the bend specimen.

deformation i.e. bending, and the material microstructure on ductile fracture of DP steel sheets are discussed. Parametric studies are also carried out to explore the effect of material parameters that dictate the propensity of void nucleation, energy dissipated in the growth of nucleated voids prior to crack nucleation, and initial porosity on ductile fracture of DP steel sheets under bending.

2. Problem formulation and numerical method

Microstructure-based finite element modeling of deformation and fracture of DP steel sheets subjected to 90° V-bend loading conditions are carried out for a thin slice of material with dimensions, $L = 16mm$ (along x-axis), $d = 1.6mm$ (along y-axis) and $W = 0.01mm$ (along z-axis), as shown schematically in Fig. 1. The tip radius of the 90° V-bend punch is taken to be $0.1mm$. The finite element mesh consists of $22,920$ twenty node brick elements giving $161,973$ nodes. For the finite element mesh a single element through the width, W (along z-axis), of the specimen is used. A very fine uniform in-plane ($x-y$ plane) mesh is used in a $1.6mm \times 0.8mm$ region (marked as *abcd* in Fig. 1) near the free surface of the bend specimen with in-plane element dimension $10\mu m \times 10\mu m$. The element dimension in the fine mesh region, $e = 10\mu m$, serves as a normalization length-scale.

The finite element calculations are carried out using our in-house data parallel finite element code as in Srivastava et al. (2014, 2017); Osovski et al. (2015b, a); Nsouglo et al. (2018); Liu et al. (2019). The finite element code is based on the dynamic principle of virtual work using a finite deformation Lagrangian convected coordinate formulation. The displacement and velocity boundary conditions imposed on the region analyzed follows the configuration shown schematically in Fig. 1. The y-displacement of the specimen is constraint at locations, $y = 0$, $x = -7.5mm$ and $y = 0$, $x = 7.5mm$ in the reference configuration. Overall plane strain conditions are imposed on $z = 0$ and $z = W$ surfaces of the bend specimen. The tip of the 90° V-bend punch is initially in contact with the bend specimen at $y = 1.6mm$ and $x = 0$. Although, calculations are based on the dynamic principle of virtual work for numerical convenience, the focus is on quasi-static response, hence to minimize the wave effects a time varying velocity, $V_y(t)$, in the negative y direction is applied to the tip of the punch that follows the relation:

$$V_y(t) = \begin{cases} V_y^0 t \big/ t_r & \text{if} \quad t \le t_r \\ V_y^0 & \text{if} \quad t > t_r \end{cases} \tag{1}$$

where, t is the analysis time, t_r is the rise time and V_y^0 is the final velocity of the punch for $t > t_r$. In the calculations, $t_r = 1.0 \times 10^{-4} s$ and $V_y^0 = 3.0 \times 10^3 mm/s$ (along the negative y direction) is used. As the deformation proceeds i.e. the tip of the punch moves in the negative y direction, additional nodes on the top surface of the specimen comes in contact with the 90° V-bend punch. These additional nodes are assigned the value of V_y which is equal to the velocity of the tip of the punch at the time of contact. Also, to all the nodes that are in contact with the punch, zero velocity along x direction, $V_x = 0$, is imposed. This corresponds to perfect sticking of the material to the punch.

As in Srivastava et al. (2014, 2017); Osovski et al. (2015b, a); Liu et al. (2019), eight point Gaussian integration is used in each twenty-node element for integrating the internal force contributions and twenty-seven point Gaussian integration is used for the element mass matrix. Lumped masses are used so that the mass matrix is diagonal. The discretized equations are integrated using the

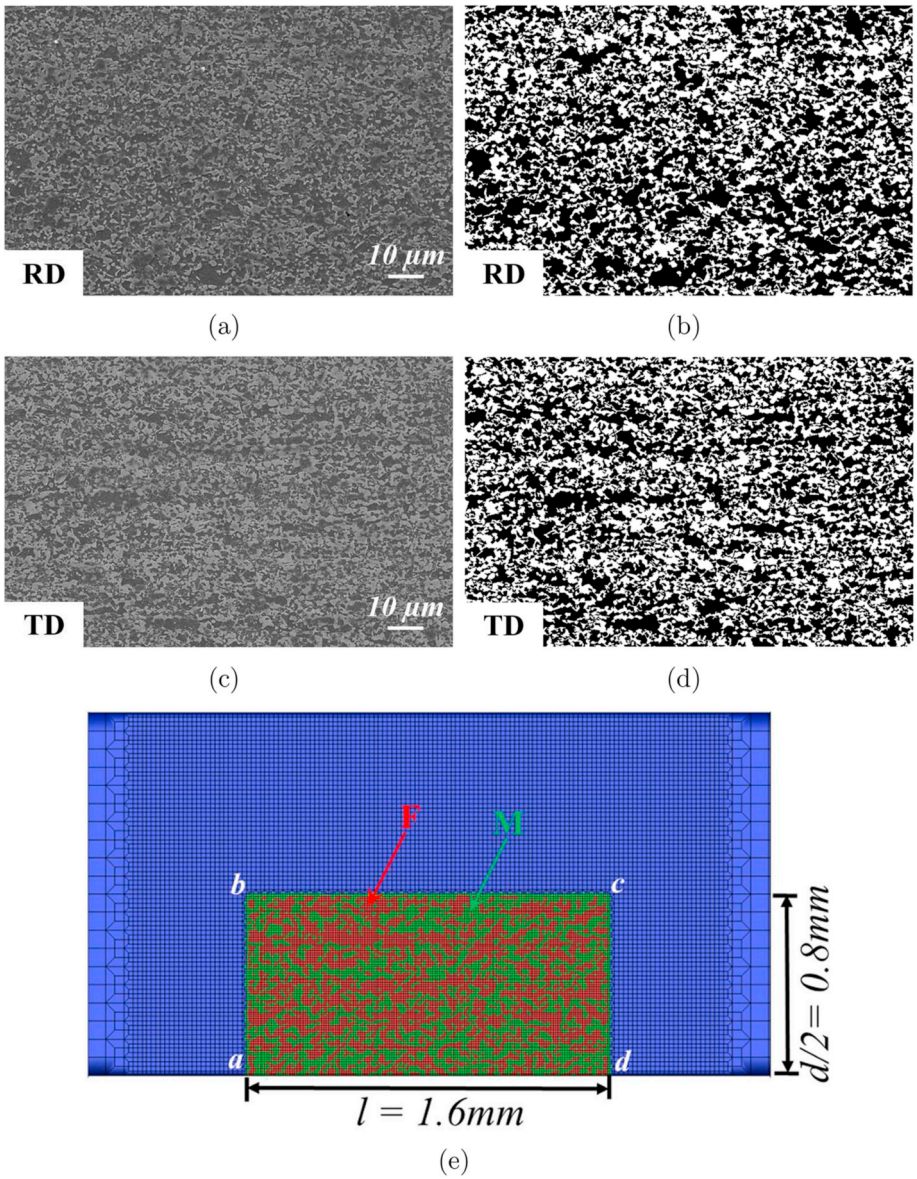

Fig. 2. (a) A representative (secondary electron) SEM image and (b) its binary version of the microstructure taken from the rolling direction (RD) cross-section of the DP steel under consideration. (c) A representative SEM image and (d) its binary version of the microstructure taken from the transverse direction (TD) cross-section of the DP steel under consideration. (e) A zoomed view of the finite element mesh near the free surface of the bend specimen showing the discretely modeled, ferrite (F) and martensite (M), phases of the DP steel microstructure in the region marked as *abcd*.

explicit Newmark β-method with $\beta = 0$ (Belytschko et al., 1976). The constitutive updating is based on the rate tangent modulus method proposed in Peirce et al. (1984), while material failure is implemented via the element vanishing technique proposed in Tvergaard (1982a).

2.1. Microstructure modeling

Microstructure-based finite element modeling of DP steel sheets under realistic boundary conditions requires modeling the entire specimen and the microstructure within. In theory, it is possible to carry out microstructure-based finite element modeling of an entire specimen with all of its microstructural details. However, the mesh density required to discretely model micron-size microstructural features in a bending specimen of dimensions in centimeters would make the finite element calculations prohibitively time consuming. Hence, we discretely model the material microstructure in a small area but large enough to capture nucleation and coalescence of micro-cracks near the free surface of the specimen, as shown in Fig. 2. To this end, secondary electron SEM images of chemically etched metallographic specimens of a DP1000 steel sheet are digitized via Marker-Controlled Watershed Segmentation method (MATLAB,

Table 1
Average size of ferrite and martensite phases along x (specimen length) and y (specimen depth) axes in RD and TD cross-sections of the DP steel under consideration. The values in the units of μm are for the 'real' microstructure while the values in the units of e (normalization length-scale) are for the microstructure 'modeled'.

Orientation	Phase	Along x-axis	Along y-axis	Aspect ratio
RD	Ferrite	$2.09\mu m$ ($4.18e$)	$1.75\mu m$ ($3.5e$)	≈ 1.19
	Martensite	$1.76\mu m$ ($3.52e$)	$1.52\mu m$ ($3.04e$)	≈ 1.15
TD	Ferrite	$1.98\mu m$ ($3.96e$)	$1.63\mu m$ ($3.26e$)	≈ 1.21
	Martensite	$1.72\mu m$ ($3.44e$)	$1.49\mu m$ ($2.98e$)	≈ 1.15

R2017b) as shown in Fig. 2 (a)–(b) and (c)-(d). The Marker-Controlled Watershed Segmentation method is used in lieu of image thresholding because of the limited contrast between the constituent phases of the DP steel in an SEM image. The basic procedure of Marker-Controlled Watershed Segmentation method involves, computing a segmentation function, computing foreground and background markers, modifying the segmentation function so that it only has minima at the foreground and background marker locations, and finally computing the watershed transform of the modified segmentation function. All these steps can be carried out using the built-in Image Processing Toolbox™ in MATLAB (MATLAB, R2017b). Next, the SEM image is magnified by 20X to 'artificially' increase the feature sizes to allow us to choose a reasonable mesh size to resolve the details of the microstructure. The 20X magnification increases an actual length of $1\mu m$ to $20\mu m$ (or in terms of the normalization length-scale, e, it is simply $2e$), while keeping the overall volume fraction of the phases fixed. The digitized and magnified microstructures are then superimposed on the mesh in the region marked as *abcd* in Figs. 1 and 2(e), and material properties corresponding to respective microstructural features are assigned based on material (Gaussian) integration points rather than finite elements. Discretizing material microstructure based on integration points allows us to smoothly resolve the interphase boundaries as shown in Fig. 2(e). The region outside *abcd* in the bend specimen are assigned material properties corresponding to the overall (homogenized) mechanical response of the DP steel under consideration.

In this work, the microstructure of the DP steel in both RD and TD cross-sections, Fig. 2(a)-(b) and (c)–(d) respectively, are considered. The average size of ferrite and martensite phases along x (specimen length) and y (specimen depth) axes in the RD and TD cross-sections are given in Table 1. In the DP steel under consideration, on average, the aspect ratio of the martensite phase in both RD and TD cross-sections are roughly the same. The average aspect ratio of the ferrite phase, however, is slightly greater in the TD cross-section as compared to the RD cross-section. Hereafter, RD (TD) refers to bend specimens with bending axis parallel to the RD (TD) of the DP steel sheet or the microstructure modeled in the region *abcd*, Fig. 2(e), is the microstructure corresponding to the RD (TD) cross-section. For both RD and TD bend specimens five microstructures taken from five locations on the respective cross-sections of the DP sheet steel under consideration have been analyzed.

2.2. Constitutive framework

The constitutive framework used here is the modified Gurson elastic-viscoplastic constitutive relation for a progressively cavitating solid (Gurson, 1975; Tvergaard and Needleman, 1984; Chu and Needleman, 1980) with the flow potential having the form

$$\phi = \frac{\sigma_e^2}{\bar{\sigma}^2} + 2q_1 f^* \cosh\left(\frac{3q_2\sigma_h}{2\bar{\sigma}}\right) - 1 - (q_1 f^*)^2 = 0 \tag{2}$$

where $q_1 = 1.5$, $q_2 = 1.0$ are parameters introduced in Tvergaard (1981, 1982b), f^* is the effective void volume fraction, $\bar{\sigma}$ is the matrix flow strength, and

$$\sigma_e^2 = \frac{3}{2}\boldsymbol{\sigma}' : \boldsymbol{\sigma}' \quad , \quad \sigma_h = \frac{1}{3}\boldsymbol{\sigma} : \mathbf{I} \quad , \quad \boldsymbol{\sigma}' = \boldsymbol{\sigma} - \sigma_h \mathbf{I} \tag{3}$$

For $f^* = 0$, the flow potential in Eq. (2) reduces to the Mises flow potential. The function f^*, introduced in Tvergaard and Needleman (1984), is given by

$$f^* = \begin{cases} f, & f < f_c \\ f_c + (1/q_1 - f_c)(f - f_c)/(f_f - f_c), & f \geq f_c \end{cases} \tag{4}$$

where, f_c is the critical void volume fraction to void coalescence and f_f is the void volume fraction at failure. The value of $f_f = 0.2$ is taken for all the calculations. When the value of the void volume fraction, f, at an integration point reaches $0.9f_f$, the value of f is kept fixed so that the material deforms with a very low flow strength. The entire element is taken to vanish following the technique proposed in Tvergaard (1982a) when three of the eight integration points in the element have reached this stage as in Srivastava et al. (2014, 2017); Osovski et al. (2015b, a); Liu et al. (2019).

The rate of deformation tensor is taken as the sum of an elastic part, $\mathbf{d}^e = \mathbf{L}^{-1} : \overset{\circ}{\boldsymbol{\sigma}}$, and a viscoplastic part, $\mathbf{d}^p$, so that

$$\mathbf{d} = \mathbf{L}^{-1} : \overset{\circ}{\boldsymbol{\sigma}} + \mathbf{d}^p \tag{5}$$

Here, $\overset{\circ}{\boldsymbol{\sigma}}$ is the Jaumann rate of Cauchy stress and $\mathbf{L}$ is the tensor of isotropic elastic moduli. The plastic part of the strain rate, $\mathbf{d}^p$, is given

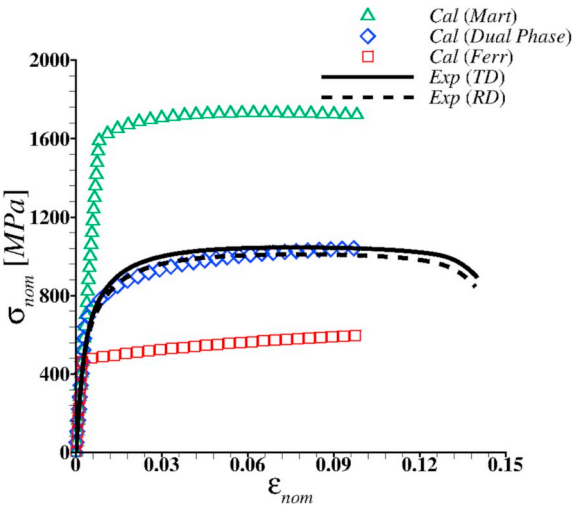

Fig. 3. Comparison of uniaxial tensile nominal stress (σ_{nom}) - strain (ε_{nom}) response of the DP steel sheet obtained from uniaxial tensile tests with tensile axis parallel to rolling direction, *Exp*(*RD*), and transverse direction, *Exp*(*TD*), and finite element calculation using the calibrated constitutive relation, Eq. (7), for fully dense ($f = 0$ throughout the deformation) homogenized DP steel sheet, *Cal*(*Dual Phase*). The extracted uniaxial tensile, σ_{nom} - ε_{nom}, curves of fully dense ferrite, *Cal*(*Ferr*), and martensite, *Cal*(*Mart*), phases present in the DP steel under consideration are also shown in the figure.

by Pan et al. (1983).

$$\mathbf{d}^p = \left[\frac{(1-f)\bar{\sigma}\dot{\bar{\varepsilon}}}{\boldsymbol{\sigma} : \frac{\partial \phi}{\partial \boldsymbol{\sigma}}}\right] \frac{\partial \phi}{\partial \boldsymbol{\sigma}} \tag{6}$$

The matrix plastic strain rate, $\dot{\bar{\varepsilon}}$, is given by

$$\dot{\bar{\varepsilon}} = \dot{\varepsilon}_0 \left[\frac{\bar{\sigma}}{g(\bar{\varepsilon})}\right]^{1/m} \quad , \quad g(\bar{\varepsilon}) = \sigma_0 \left[1 + \bar{\varepsilon}/\varepsilon_0\right]^N \tag{7}$$

with $\bar{\varepsilon} = \int \dot{\bar{\varepsilon}} dt$. In Eq. (7), $\dot{\varepsilon}_0$ is the reference strain rate, m is the strain rate sensitivity exponent, σ_0 is the initial flow strength, ε_0 is reference strain and N is the strain hardening exponent.

The evolution of the void volume fraction is governed by

$$\dot{f} = (1-f)\mathbf{d}^p : \mathbf{I} + \dot{f}_{nucl} \tag{8}$$

where the first term on the right hand side of Eq. (8) accounts for void growth and the second term accounts for void nucleation. The value of f in the undeformed material i.e. value of f at time, $t = 0$, represents the initial void volume fraction or porosity, f_0. The void nucleation rate, $\dot{f}_{nucl}$, is related to the accumulated plastic strain, $\bar{\varepsilon}$, and plastic strain rate, $\dot{\bar{\varepsilon}}$, by (Chu and Needleman, 1980)

$$\dot{f}_{nucl} = \frac{f_N}{s_N\sqrt{2\pi}} \exp\left[-\frac{1}{2}\left(\frac{\bar{\varepsilon} - \varepsilon_N}{s_N}\right)^2\right] \dot{\bar{\varepsilon}} \tag{9}$$

with f_N, ε_N, and s_N being constitutive parameters. Eq. (9) is based on the hypothesis that there is a mean equivalent plastic strain, ε_N, for void nucleation and that this nucleation strain is distributed in a normal fashion about the mean with a standard deviation, s_N. The parameter f_N determines the maximum void volume fraction nucleated at a material (Gaussian) integration point.

2.3. Constitutive parameter identification

The constitutive framework described in Section 2.2 contains several constitutive (material) parameters. The values of these parameters must be determined for the overall DP microstructure as well as for the individual constituent phases, ferrite and martensite, in order to carry out microstructure-based finite element modeling. To determine the values of the constitutive parameters that best represent the overall stress-strain response of the fully dense ($f = 0$ throughout the deformation) DP steel sheet, we first fix the values of Young's modulus, E, Poisson's ratio, ν, and strain rate sensitivity exponent, m. The value of m is fixed following the work of Srivastava et al. (2016). The values of the remaining constitutive parameters, initial flow strength, σ_0, strain hardening exponent, N, reference strain, ε_0, and reference strain rate, $\dot{\varepsilon}_0$, are then directly obtained using the portion of the experimental stress-strain curve

Table 2
The values of the constitutive parameters for the overall (homogenized) DP steel, and for the individual constituent phases, ferrite and martensite, present in the DP microstructure under consideration.

Parameters	Dual Phase	Ferrite	Martensite
Young's modulus, $E(Gpa)$	200	200	200
Poisson's ratio, ν	0.3	0.3	0.3
Initial flow strength, $\sigma_0(MPa)$	610	430	1450
Strain hardening exponent, N	0.14	0.35	0.06
Reference strain, ε_0	0.00175	0.06	0.006
Strain rate sensitivity exponent, m	0.01	0.01	0.01
Reference strain rate, $\dot{\varepsilon}_0(s^{-1})$	0.1	0.01	0.01

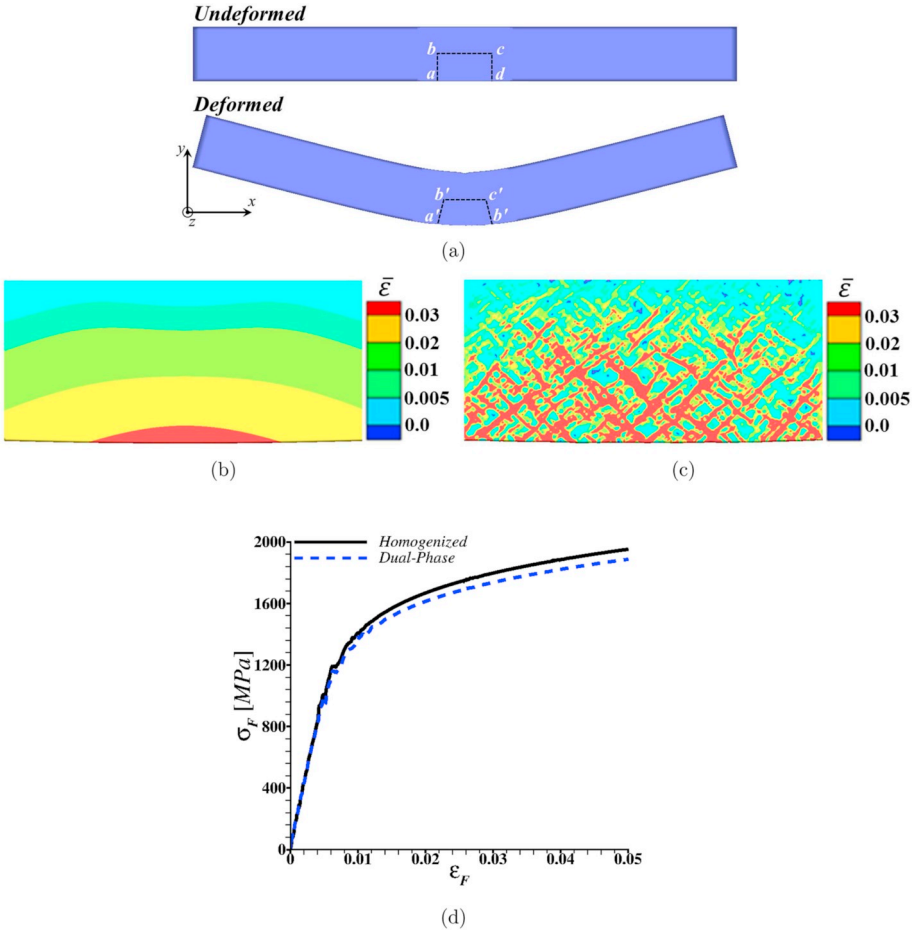

Fig. 4. (a) The undeformed and deformed configuration of a bend specimen subjected to a macroscopic flexural strain, $\varepsilon_F \approx 0.05$, using a 90° V-bend punch. The distribution of equivalent plastic strain, $\bar{\varepsilon}$, in the near surface region (a'b'c'd') on the tension side of the deformed bend specimen ($\varepsilon_F \approx 0.05$) with (b) homogenized material and (c) discrete DP steel microstructure in the region marked as *abcd* in (a). (d) Comparison of the macroscopic flexural stress (σ_F) - strain (ε_F) response of the bend specimen modeled as homogenized material and discrete DP steel microstructure in the region marked as *abcd* in (a).

before the onset of necking. The values of all the constitutive parameters that best represent the overall stress-strain response of the fully dense DP steel under consideration are tabulated in Table 2. A comparison of uniaxial tensile nominal stress - strain response of the industrially produced galvannealed DP1000 sheet steel under consideration and finite element calculation using the constitutive parameter given in Table 2 for fully dense DP steel sheet before the onset of necking is shown in Fig. 3.

Next, we focus on determining the values of the constitutive parameters for the fully dense ($f = 0$ throughout the deformation) constituent phases, ferrite and martensite. To this end, we first constructed a 3D representative volume element (RVE) of the DP microstructure using the procedure described in Gerbig et al. (2018); Ghoreishi et al. (2018). The DP steel sheet considered in this work

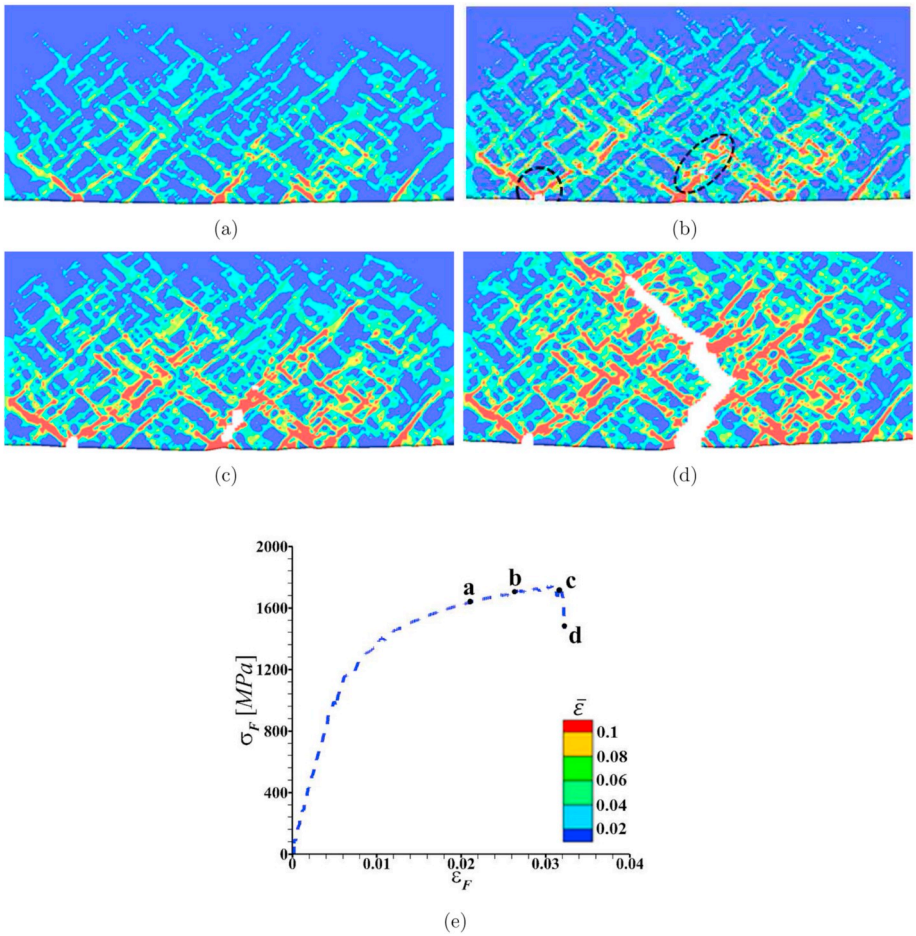

Fig. 5. (a)–(d) The distribution of equivalent plastic strain, $\bar{\varepsilon}$, in the near surface region on the tension side of the deformed bend specimen with discrete DP steel microstructure at four macroscopic flexural strain, ε_F, levels marked with letters, $a - d$, on the macroscopic flexural stress (σ_F) - strain (ε_F) curve in (e).

contains ≈ 54% ferrite and ≈ 46% martensite phase by volume. The values of the constitutive parameters, E, ν, and m are fixed a priori for both phases. The value of σ_0 for the ferrite phase is also fixed a priori based on our prior experience (Srivastava et al., 2015, 2016). In addition, the range (upper and lower bound) of the values of N for the martensite phase is chosen to represent negligible strain hardening in the martensite phase based on our prior experience. Following this, an iterative optimization procedure was used to determine the values of the constitutive parameters, N, ε_0, and $\dot{\varepsilon}_0$ for the ferrite phase and σ_0, N, ε_0, and $\dot{\varepsilon}_0$ for the martensite phase, that minimizes the mean squared error between the uniaxial stress-strain response of the RVE and prediction using the constitutive parameter given in Table 2 for fully dense DP steel. The iterative optimization scheme was implemented as a MATLAB function. The MATLAB function carries out the finite element calculations of uniaxial tensile test of the RVE; calculates the average mean squared error of the difference between predicted and target stress-strain data; and minimizes the error by adjusting the values of the constitutive parameters following the Nelder-Mead simplex algorithm. The values of all the constitutive parameters for both constituent phases are tabulated in Table 2, and the uniaxial nominal stress-strain response of the two fully dense constituent phases obtained using these parameters are shown in Fig. 3.

Apart from the constitutive parameters needed to model the mechanical response of the fully dense material that are given in Table 2, the constitutive framework detailed in Section 2.2 also contains parameters associated with the modified Gurson model. These parameters are, initial porosity, f_0, critical void volume fraction to void coalescence, f_c, and the three parameters, f_N, s_N and ε_N associated with the void nucleation criteria in Eq. (9). Note, damage is only considered to take place in the region marked *abcd* in Fig. 1 or Fig. 2(e) where the constituent phases, ferrite and martensite, of the DP steel are discretely modeled. So that the constitutive parameters corresponding to the modified Gurson model are only needed for the ferrite and martensite phase and not for the overall (homogenized) DP steel. Following the work of Gerbig et al. (2018), we take $f_0 = 0$ in the ferrite phase and $f_0 = 0.002$ in the martensite phase. The values of the other four parameters, $f_c = 0.1$, $f_N = 0.04$, $s_N = 0.01$, and $\varepsilon_N = 0.2$, are initially taken to be same for both phases. Parametric studies are carried out to explore the effect of variation in the values of f_0, f_c and ε_N for both phases on the bendability of DP steel sheets.

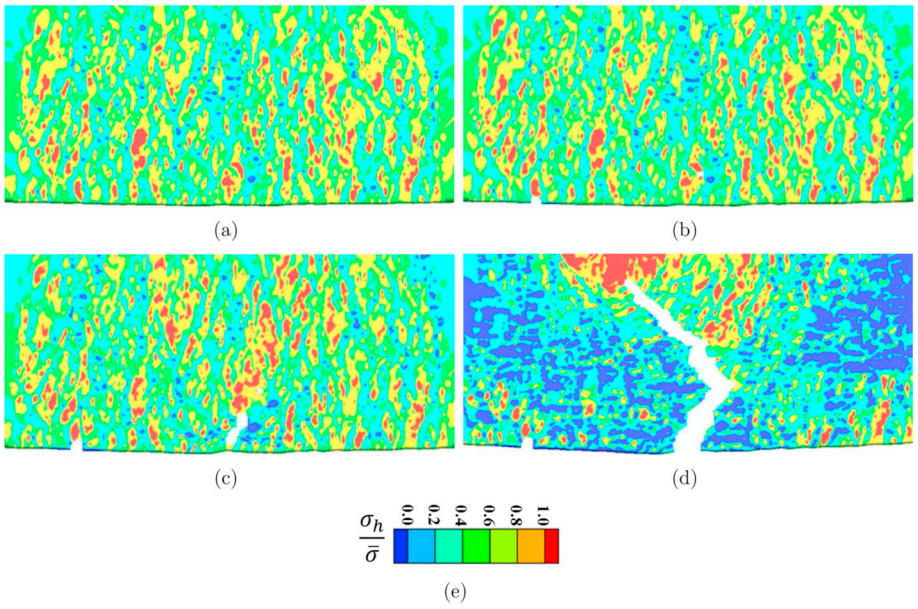

Fig. 6. The distribution of stress triaxiality (ratio of hydrostatic stress and matrix flow strength), $\sigma_h/\bar{\sigma}$, in the near surface region on the tension side of the deformed bend specimen with discrete DP steel microstructure at four macroscopic flexural strain, ε_F, levels marked with letters, $a-d$, on the macroscopic flexural stress (σ_F) - strain (ε_F) curve in Fig. 5(e).

3. Numerical results

The initial undeformed and deformed configuration of a bend specimen subjected to a macroscopic flexural strain, $\varepsilon_F \approx 0.05$, using a 90° V-bend punch are shown in Fig. 4(a). The distribution of the equivalent plastic strain ($\bar{\varepsilon}$) in the region $a'b'c'd'$ on the tension (convex) side of the deformed bend specimen at $\varepsilon_F \approx 0.05$ for the scenario where the entire bend specimen is modeled as homogenized DP steel is shown in Fig. 4(b). Similarly, the distribution of $\bar{\varepsilon}$ in the region $a'b'c'd'$ for the scenario where the DP steel microstructure is discretely modeled in the region *abcd* and the rest of the specimen is modeled as homogenized DP steel is shown in Fig. 4(c). Finally, the macroscopic flexural stress (σ_F) - strain (ε_F) response of the bend specimen modeled as homogenized material and discrete DP steel microstructure in the region *abcd* are compared in Fig. 4(d). The values of σ_F and ε_F are estimated as,

$$\sigma_F = \frac{3F_y L}{2Wd^2}, \quad \varepsilon_F = \frac{6\delta_y d}{L^2} \tag{10}$$

where, F_y is the reaction force on the punch and δ_y is the deflection of the tip of the punch along the loading direction.

The results in Fig. 4 correspond to the calculations with $f = 0$ everywhere in the specimen and throughout the deformation history i.e. the initiation and evolution of ductile damage are suppressed. As shown in Fig. 4(d), in the absence of any damage, the macroscopic σ_F - ε_F response of the homogeneous bend specimen is very similar to the response of the heterogeneous microstructure. This shows that the overall deformation response of DP steel sheets under bending is not very sensitive to the details of local microstructural length-scales. The comparison of σ_F - ε_F curves in Fig. 4(d) also shows that the extracted local mechanical properties of ferrite and martensite phases are correct. The discreteness of the local microstructure of the DP steel, however, does affect the local distribution of the field variables. For example, the local distribution of $\bar{\varepsilon}$, is very different in Fig. 4(c) compared to Fig. 4(b). In the homogeneous bend specimen, bending induces a single length-scale that leads to a smooth gradient in the distribution of $\bar{\varepsilon}$, Fig. 4(b) whereas, in the bend specimen with DP microstructure the interlacing of the length-scales induced by bending and DP microstructure results in extremely complex and heterogeneous distribution of $\bar{\varepsilon}$, Fig. 4(c).

3.1. Micromechanism of ductile fracture

The distribution of $\bar{\varepsilon}$ in the near surface region on the tension side of the deformed bend specimen with discrete DP steel microstructure undergoing damage initiation and growth at four ε_F values are shown in Fig. 5(a)-(d). The corresponding macroscopic σ_F - ε_F curve is shown in Fig. 5(e). The ε_F values corresponding to Fig. 5(a)–(d) are marked with letters $a-d$ on σ_F - ε_F curve in Fig. 5(e). The 'white' regions in Fig. 5(a)–(d) mark the locations of micro-crack nucleation and growth. Similarly, the distribution of stress triaxiality, $\sigma_h/\bar{\sigma}$, at four ε_F values corresponding to $a-d$ on σ_F - ε_F curve in Fig. 5(e) are shown in Fig. 6(a)-(d).

As shown in Figs. 5(a) and 6(a), in bend specimens with discretely modeled DP steel microstructure, the interlacing of length-scales induced by bending and material microstructure results in extremely heterogeneous distribution of strains and stresses even before the onset of any ductile damage. The length-scale induced by bending results in a gradient in the distribution of $\bar{\varepsilon}$ with the value of $\bar{\varepsilon}$ being

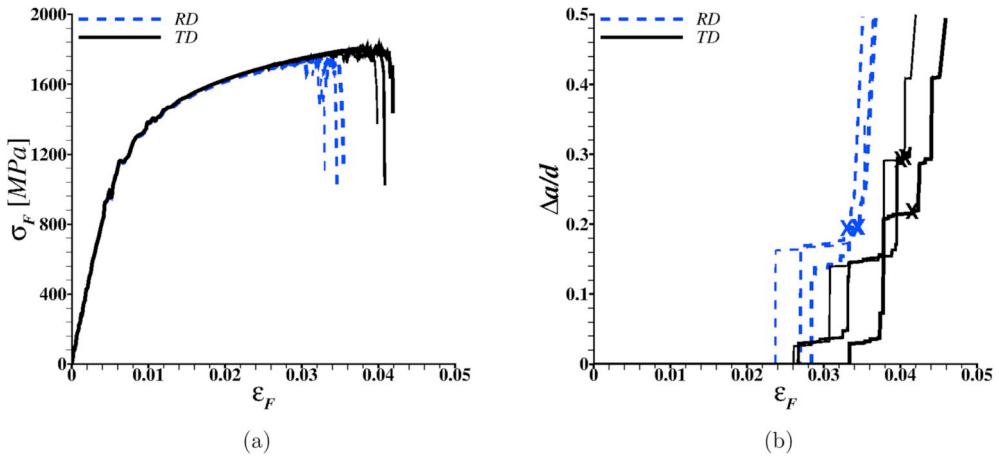

Fig. 7. (a) Macroscopic flexural stress (σ_F) - strain (ε_F) response of bend specimens with discrete DP steel microstructures corresponding to RD (rolling direction) and TD (transverse direction) cross-sections. (b) Evolution of normalized crack length, $\Delta a/d$, with ε_F. The values of $\Delta a/d$ at ε_F corresponding to drop in the value of σ_F in (a) is marked with cross in (b). For both RD and TD bend specimens, results for three microstructures taken from three locations on the respective cross-sections of the DP steel sheet are presented in (a) and (b).

greater at the surface, while due to the discreteness of the DP microstructure the value of $\bar{\varepsilon}$ is greater in the soft phase i.e. ferrite. Additionally, due to the local constrained imposed by the distribution of the hard phase i.e. martensite, the value of σ_h is greater in the ferrite phase while the value of $\bar{\sigma}$ is greater in the martensite phase. This results in greater $\sigma_h/\bar{\sigma}$ values in the ferrite phase.

With continued bending deformation, Fig. 5(b), the value of $\bar{\varepsilon}$ localizes in bands inclined at $\approx 45^\circ$ with the loading axis, and the free surface on the tension side undergoes surface roughening. The 'hot spots' of $\sigma_h/\bar{\sigma}$ are however seems to be randomly distributed, Fig. 6 (b). The interaction of $\bar{\varepsilon}$ localization bands and surface roughening results in nucleation of surface (marked with dashed-line circle) and sub-surface (marked with dashed-line ellipse) micro-cracks that are away from the center of the specimen, Fig. 5(b). Note that in a homogeneous isotropic material under bending the cracks nucleate at the center of the specimen. The relatively large surface micro-crack that nucleates away from the center of the specimen does not seem to grow but with continued bending deformation the small sub-surface micro-crack marked with the ellipse in Fig. 5(b) grows towards the free surface along one of the $\bar{\varepsilon}$ localization band, Fig. 5 (c). The presence of this large sub-surface micro-crack also results in redistribution of the 'hot spots' of $\sigma_h/\bar{\sigma}$, Fig. 6(c). The continued bending deformation, hereafter, results in growth of this micro-crack towards the interior of the specimen, Fig. 5(d), as well as drop in the macroscopic σ_F value, Fig. 5(e). As shown in Figs. 5(d) and 6(d), the crack initially grows away from the loading axis but with continued bending deformation the crack deflects back towards the loading axis.

3.2. *Effect of RD and TD microstructures*

Here, we analyze the effect of RD and TD microstructures on the bend fracture of DP steel sheets. The calculated macroscopic σ_F - ε_F curves for bending along RD and TD directions are shown in Fig. 7(a). The calculations show that the deformation response of RD and TD specimens under bending prior to fracture i.e. drop in the value of σ_F are the same. The value of ε_F corresponding to drop in the value of σ_F is however greater for TD specimens than for RD specimens. The three σ_F - ε_F curves for bending along RD and TD directions shown in Fig. 7(a) are for three local microstructures taken from different locations on the respective cross-sections of the DP steel sheet. In all the calculations, RD or TD, the values of the constitutive parameters, overall volume fraction of the constituent phases, the specimen geometry and the loading conditions are the same so that the difference in the response of RD and TD specimens under bending is solely due to the variations in the topological features of the microstructure in RD and TD cross-sections. The evolution of the normalized crack length, $\Delta a/d$, with ε_F, is shown in Fig. 7(b). As shown in Fig. 7(b), the value of ε_F at first crack nucleation is on average greater for TD specimens than RD specimens. Furthermore, the evolution of Δa with ε_F is faster for RD specimens compared to TD specimens, resulting in poor damage tolerance and bend fracture resistance for RD specimens compared to TD specimens.

Next, we analyze the distributions of $\bar{\varepsilon}$ along a line in the subsurface of the tension side of bend specimens deformed to a macroscopic $\varepsilon_F \approx 0.03$. The distribution is taken along a line parallel to the length of the specimen and at a depth of $y_0/d \approx 0.0325$ from the tension side of the specimen in the undeformed configuration. The distribution of $\bar{\varepsilon}$ along this line in a RD specimen is shown in Fig. 8(a) and in a TD specimen is shown in Fig. 8(b). Several general observations can be made from Fig. 8(a) and (b): (i) the value of $\bar{\varepsilon}$ in the ferrite phase is in general greater than the value of $\bar{\varepsilon}$ in the martensite phase, (ii) the peaks in the value of $\bar{\varepsilon}$ in the ferrite phases lies close to the ferrite-martensite interface, (iii) not all peaks in the value of $\bar{\varepsilon}$ in the ferrite (or in the martensite) region have the same amplitude, (iv) the peaks in the value of $\bar{\varepsilon}$ in the ferrite (or in the martensite) region with high amplitudes do not lie at the center of the bend specimen (contrary to what is expected for a homogeneous material undergoing bending), and (v) the number of peaks in the value of $\bar{\varepsilon}$ in the RD specimen is greater than the number of peaks in the TD specimen.

Similarly, the distribution of porosity, f, along the same line in the subsurface of the tension side of RD and TD bend specimens are shown in Fig. 8(c) and (d), respectively. In the calculations, void nucleation in both phases is assumed to follow a plastic strain

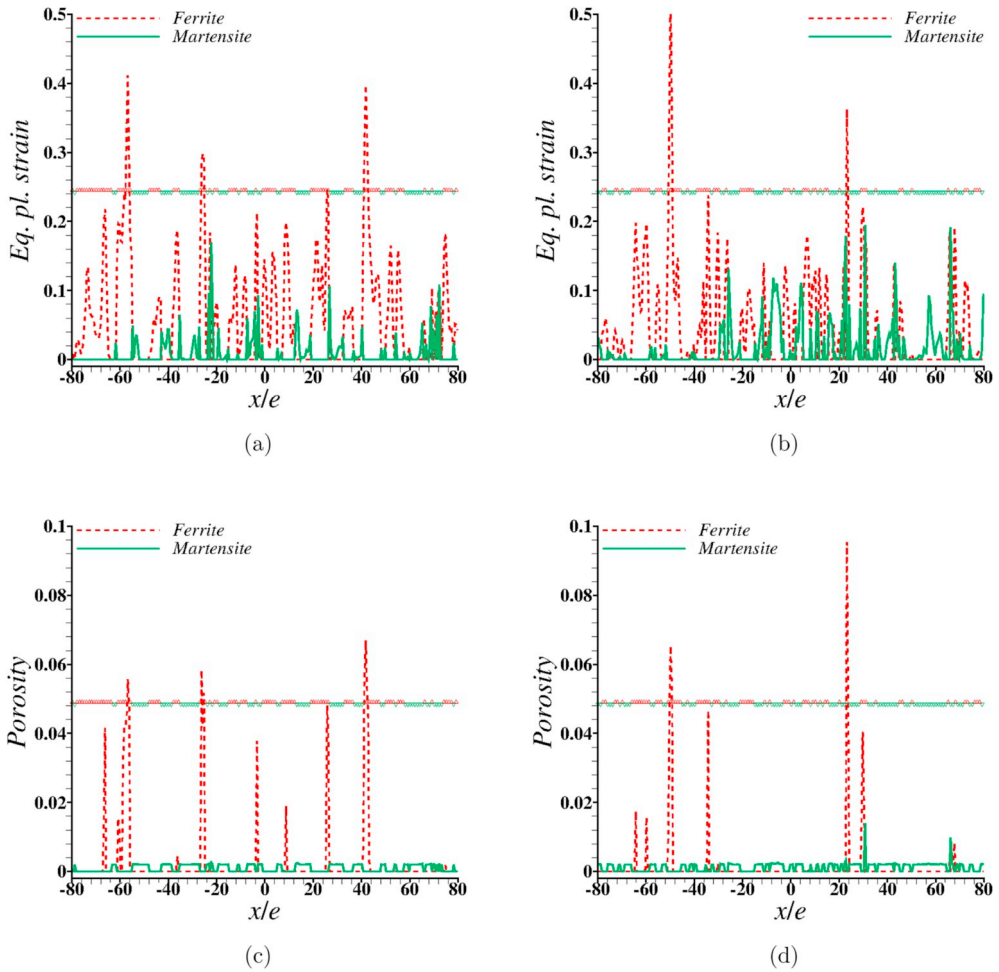

Fig. 8. The distribution of equivalent plastic strain, $\bar{\varepsilon}$, at a macroscopic flexural strain, $\varepsilon_F \approx 0.03$, along a line in the subsurface of the tension side of bend specimens with discrete DP steel microstructures corresponding to (a) RD and (b) TD cross-sections. Similar distribution of porosity, f, at $\varepsilon_F \approx 0.03$ in (c) RD and (d) TD bend specimens. The line profile is taken along a line parallel to the length of the specimen (along x-axis) and at a depth of $y_0/d \approx 0.0325$ from the tension side of the specimen in the undeformed configuration. The location, $x/e = 0$, corresponds to the center of the bend specimen. The respective constituent phase along the line (i.e. at an x/e value) are marked with horizontally arranged symbols: *delta* for ferrite phase and *gradient* for martensite phase.

controlled nucleation criteria, Eq. (9). So that the observed peaks in the value of f in the ferrite phase near the ferrite-martensite interface shown in Fig. 8(c) and (d) are consistent with the distribution of $\bar{\varepsilon}$ shown in Fig. 8(a) and (b). The growth of the nucleated voids, however, strongly depend on the local stress state thus not all the locations (corresponding to ferrite phase) where a peak in the value of $\bar{\varepsilon}$ is observed in Fig. 8(a) and (b) contains a peak in the value of f in Fig. 8(c) and (d). Nevertheless, similar to the distribution of $\bar{\varepsilon}$ the number of peaks in the value of f in the RD specimen is greater than the number of peaks in the TD specimen. Recall, in the calculations it is assumed that the initial porosity in the ferrite phase is zero while the martensite phase contains a small amount of initial porosity, $f_0 = 0.002$. Despite the presence of initial porosity, the value of f in the martensite phase is significantly less than that in the ferrite phase at least up to $\varepsilon_F \approx 0.03$ i.e. prior to significant micro-cracking in the specimen.

To further understand the effect of RD and TD microstructures on the bend fracture of DP steel sheets, we determine the contribution to the plastic strain and damage from each of the phases present in the DP steel at various macroscopic ε_F levels. To this end, we define the $\bar{\varepsilon}^{Phase}$ and f^{Phase} in each phase as,

$$\bar{\varepsilon}^{Phase} = \frac{1}{V_{Phase}} \sum_{EL \in Phase} \bar{\varepsilon}^{(k)} V^{(k)}, \qquad f^{Phase} = \frac{1}{V_{Phase}} \sum_{EL \in Phase} f^{(k)} V^{(k)} \tag{11}$$

where the sum is taken over all the elements (*ELs*) within one of the two phases, $V^{(k)}$ is the volume of the k^{th} element, $\bar{\varepsilon}^{(k)}$ and $f^{(k)}$ are the equivalent plastic strain and porosity computed at the centroid of the k^{th} element, and V_{Phase} is the total volume of the phase present in the microstructure in the region marked as *abcd* in Fig. 2(e). We then define the fractional contribution to the total $\bar{\varepsilon}$ and f from each

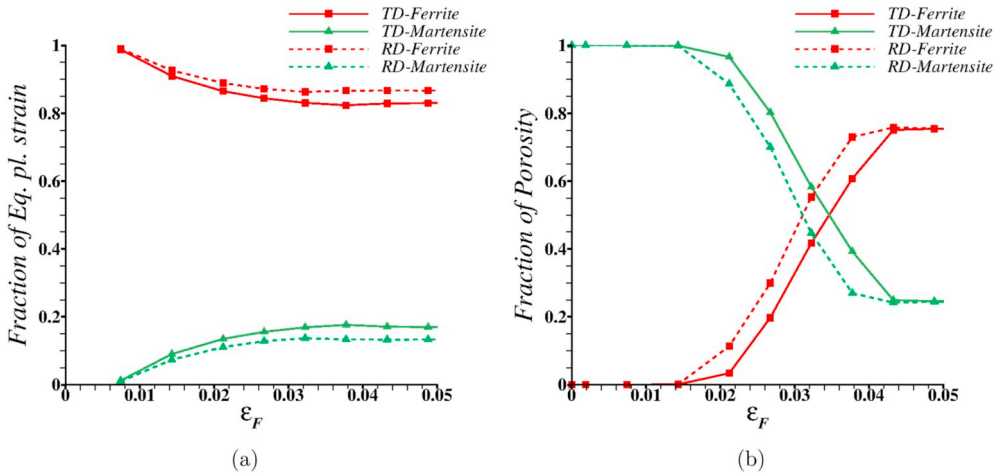

Fig. 9. Partitioning of (a) equivalent plastic strain, $\bar{\varepsilon}$, and (b) porosity, f, among the two constituent phases, ferrite and martensite, with macroscopic flexural strain, ε_F, in the bend specimens with discrete DP steel microstructures corresponding to RD and TD cross-sections.

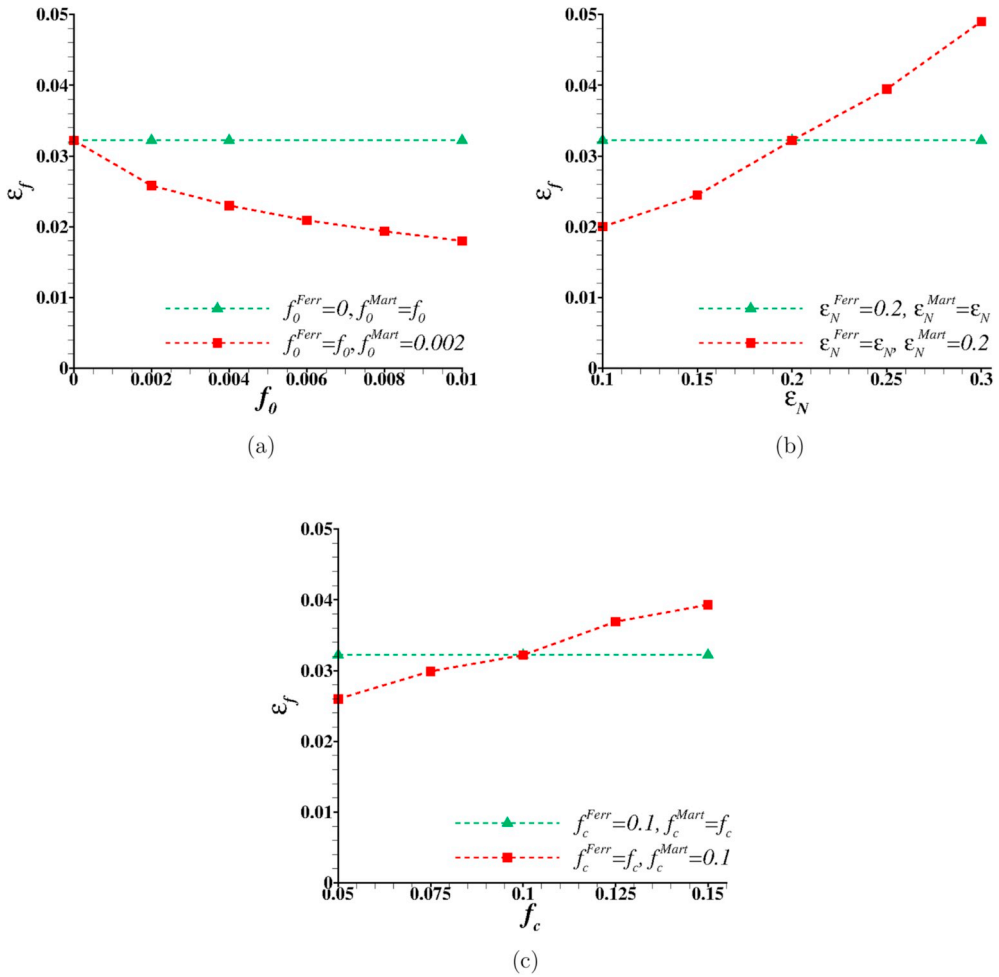

Fig. 10. The effect of variation in (a) initial porosity, f_0, (b) mean equivalent plastic strain to void nucleation, ε_N, and (c) critical void volume fraction to void coalescence, f_c, in the two constituent phases, ferrite (superscript *Ferr*) and martensite (superscript *Mart*), of a DP steel microstructure corresponding to RD cross-section on macroscopic flexural strain at failure, ε_f.

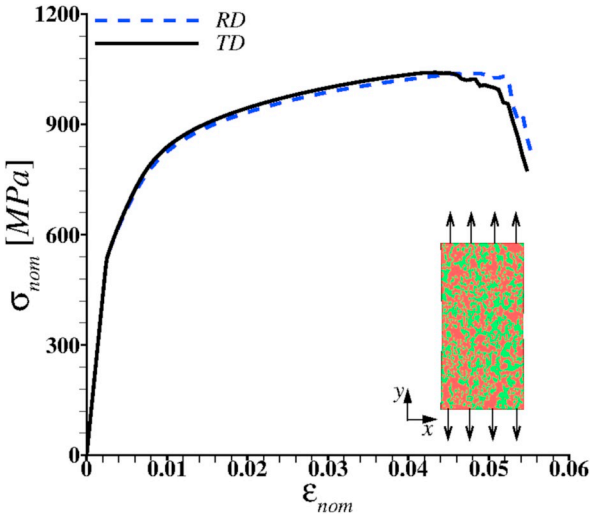

Fig. 11. Comparison of the calculated uniaxial tensile nominal stress (σ_{nom}) - strain (ε_{nom}) response of DP steel microstructures corresponding to RD (rolling direction) and TD (transverse direction) cross-sections.

phase as the ratio of $\bar{\varepsilon}^{Phase}$ and f^{Phase} to the total $\bar{\varepsilon}$ and f in both phases, respectively.

The fractional contributions of $\bar{\varepsilon}$ and f by the two phases as a function of macroscopic ε_F in RD and TD specimens are shown in Fig. 9. As shown in Fig. 9(a), the ferrite phase yields at an early stage of deformation and hence initially contributes almost all the plastic strain. Following the yielding of martensite phase the contribution to plastic strain of ferrite phase decreases gradually and that of martensite phase increases gradually. On the other hand, due to the presence of initial porosity in the martensite phase almost all the contribution to porosity initially comes from the martensite phase, Fig. 9(b). Following void nucleation in the ferrite phase the contribution to porosity of ferrite phase increases rapidly and that of martensite phase decreases rapidly. Post failure i.e. drop in σ_F values (see Fig. 7(a)), the fractional contributions of $\bar{\varepsilon}$ and f by the two phases saturates. The general trend of the fractional contributions of $\bar{\varepsilon}$ and f by the two phases as a function of ε_F is same for both RD and TD specimens. However, at a fixed ε_F prior to failure, the difference in the fractional contributions of $\bar{\varepsilon}$ by the two phases in the RD specimen is greater than that in the TD specimen, suggesting that the deformation in the TD specimen is slightly more uniform than the RD specimen. The difference in the fractional contributions of f by the two phases at a fixed ε_F in the RD and the TD specimens is simply due to the fact that damage initiation in RD specimens occurs at a lower value of ε_F than in TD specimens.

3.3. Effect of damage parameters

In this section we present the influence of ductile damage parameters on the bend fracture of DP steel sheets. The damage parameters that are considered, are the initial porosity, f_0, the mean equivalent plastic strain to void nucleation, ε_N, and the critical void volume fraction to void coalescence, f_c. The parameter, f_c, dictates the energy dissipated in the growth of nucleated voids prior to micro-crack nucleation. The parametric studies are carried out by varying the values of f_0, ε_N and f_c, one at a time, for each constituent phase. The results of this parametric study are shown in Fig. 10. As shown in the figure, a variation in the value of f_0, ε_N and f_c for the martensite phase has no effect on the macroscopic flexural strain to failure, ε_f, of DP steel sheets. On the contrary, a variation in the value of f_0, ε_N and f_c for the ferrite phase has a strong influence on the value of ε_f of DP steel sheets. Such that an increase in f_0 results in a decrease in ε_f while an increase in ε_N and f_c results in an increase in the value of ε_f.

4. Discussion

The experimental results, Fig. 3, and our microstructure-based finite element calculations, Fig. 11, both show that the uniaxial tensile deformation and fracture response of the DP sheet steel under consideration is not very sensitive to the details of the topological features of the microstructure along RD and TD. The microstructure-based finite element calculations of DP steel sheets are carried out for a thin slice of material with dimensions, $l_y = 1.6mm$, $l_z = 0.01mm$ and l_x given as,

$$l_x = l_x^0 - 2A\cos\left(2\pi\frac{y}{2l_y}\right), \qquad \left(-\frac{l_y}{2} \le y \le \frac{l_y}{2}\right) \tag{12}$$

where A is the amplitude of a small geometrical imperfection to the width, l_x^0, of the sheet specimen. The small geometrical imperfection is introduced to break the symmetry of the problem and facilitate onset of necking. The value of l_x^0 is taken to be $0.8mm$ and that of A is taken to be 1% of l_x^0. Overall plane strain conditions are imposed on $z = 0$ and $z = l_z$ surfaces of the sheet specimen and the

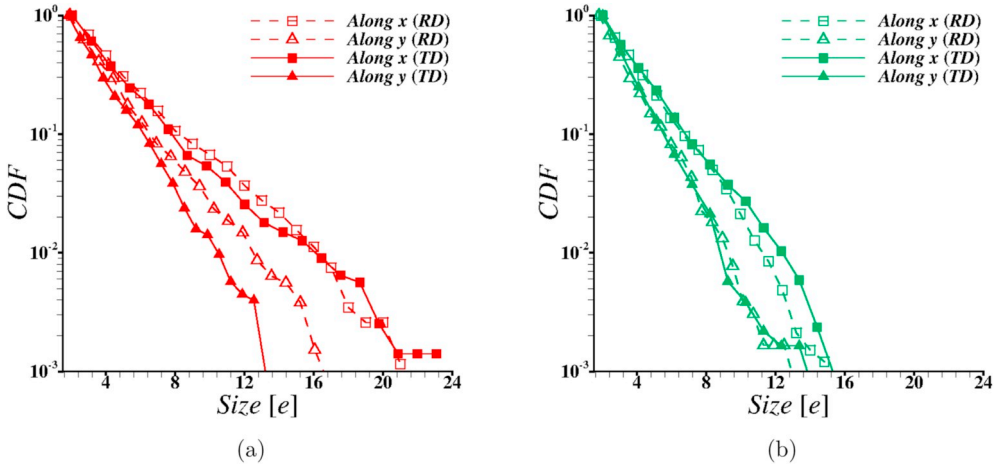

Fig. 12. The descending cumulative distribution function (CDF) of (a) the size of ferrite phase in the modeled DP steel microstructure along x (specimen length) and y (specimen depth) axes in rolling (RD) and transverse direction (TD) cross-sections, and (b) the size of martensite phase in the modeled DP steel microstructure along x and y axes in RD and TD cross-sections. The vertical axes in the plots are on logarithmic scale, and e is the normalization length-scale.

uniaxial tensile loading along the y-axis is simulated using a velocity profile similar to Eq. (1). In the calculations, both RD and TD microstructures of the DP steel sheet are modeled using the procedure described in Section 2.1 and the values of the constitutive parameters given in Section 2.3. The microstructure-based finite element calculations of DP steel sheets under uniaxial tension are carried out for several RD and TD microstructures. The results show that for the set of constitutive parameters given in Section 2.3, under uniaxial tension, the average nominal strain to fracture is 0.053 with a standard deviation of 0.0065 for RD specimens and for TD specimens it is 0.05 with a standard deviation of 0.0031.

The unstructured continuum material property descriptors such as, strength and strain hardenability, the overall microstructural parameter i.e. volume fraction of the phases, and the fracture response under uniaxial tensile loading are same for both RD and TD specimens of the DP steel under consideration. So that any analysis based on classical engineering fracture mechanics will predict the same fracture response for both RD and TD specimens under bending. Nonetheless, consistent with the experimental observations our results show that the bendability of TD specimens is greater than the bendability of RD specimens. In our calculations, the difference in the bendability of RD and TD specimens are due to the difference in the topological features of the material microstructure in RD and TD specimens of the DP steel sheet.

The descending cumulative distribution function of the sizes of ferrite and martensite phases in RD and TD specimens of the DP steel sheet modeled are shown in Fig. 12. The plots in Fig. 12 can be interpreted as displaying the probability that the size will exceed a given value on the horizontal axis. From Fig. 12, it can be seen that the probability that the size of the ferrite phase along the specimen length and that of the martensite phase along the specimen depth will exceed a given threshold is roughly the same for both RD and TD specimens. The probability that the size of the ferrite phase along specimen depth will exceed a given threshold is, however, greater for RD specimens compared to TD specimens. Similarly, the probability that the size of the martensite phase along the specimen length will exceed a given threshold is slightly greater for TD specimens compared to RD specimens. Note, that since the volume fraction of both phases are same in RD and TD specimens, Fig. 12 suggest that the probability of finding deeper ferrite-martensite interfaces are greater for RD specimens compared to TD specimens.

The subtle difference in the size of ferrite and martensite phases between RD and TD specimens of the DP steel sheet is apparently sufficient to cause a difference in the fracture response under bending. This is because bending results in an overall gradient in the distribution of $\overline{\varepsilon}$ with the value of $\overline{\varepsilon}$ being greater at the surface and within this gradient the value of $\overline{\varepsilon}$ is greater in the ferrite phase close to the ferrite-martensite interface. With continued bending deformation the value of $\overline{\varepsilon}$ localizes in bands inclined at an angle ($\approx 45^{\circ}$) with the loading axis. The peaks in the value of $\overline{\varepsilon}$ in the ferrite phase close to the ferrite-martensite interface results in void nucleation at these locations. The small difference in the topological features of the microstructure between RD and TD specimens results in: (i) fewer number of peaks in the value of $\overline{\varepsilon}$ and f near the tension side of TD specimens compared to RD specimens, and (ii) slightly smaller difference in the fractional contribution of $\overline{\varepsilon}$ by the two phases in TD specimens compared to RD specimens.

The results of our parametric studies show that in DP steel sheets under bending both the plastic deformation, and the damage nucleation and growth are concentrated in the ferrite phase. This is why, a variation in the values of the material parameters that dictate the propensity of void nucleation, energy dissipated in the growth of nucleated voids prior to crack nucleation, and initial porosity on ductile fracture of DP steel sheets under bending for martensite phase does not significantly affect the bendability of DP steel sheets. Thus, any effort to improve the bendability of DP steel sheets must focus on improving the mechanical properties of the ferrite phase.

The results presented in Fig. 7, show that even though the overall volume fraction, mechanical properties and damage parameters of the constituent phases and the orientation (RD or TD) of the bend specimens of the DP steel sheet are the same, there is a difference

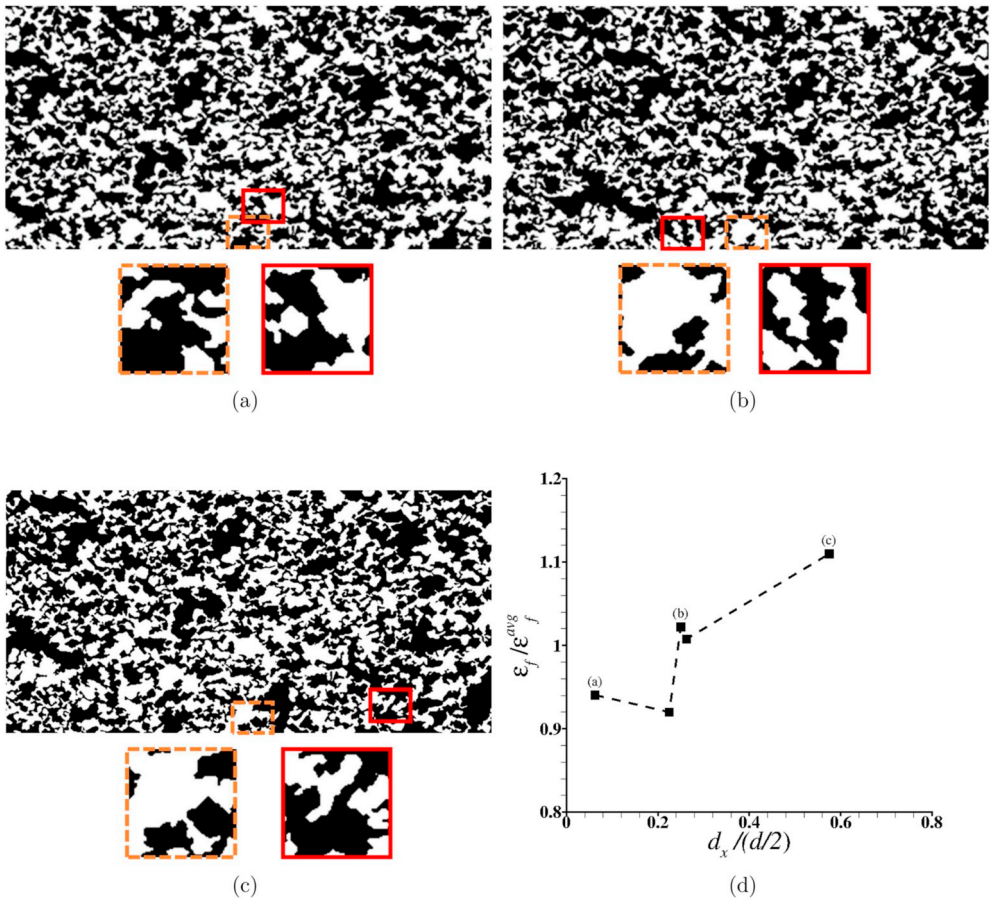

Fig. 13. (a)–(c) The distribution of ferrite (black) and martensite (white) phases in three DP steel microstructures corresponding to RD cross-section. In (a)–(c), the bottom edge of the figure is on the tension side of the bend specimen, and the dashed-line box highlights the local microstructure in the center of the bend specimen while the solid-line box highlights the microstructure at the location of first micro-crack nucleation. (d) The variation of the normalized macroscopic flexural strain at failure, $\varepsilon_f / \varepsilon_f^{avg}$, with the normalized projected (along the length of the bend specimen or x-axis) distance between the center of the bend specimen and the location of first micro-crack nucleation, $d_x /(d/2)$.

in the value of the macroscopic flexural strain to failure, ε_f, for different bend specimens. The difference in the value of ε_f for different RD (or TD) specimens stems from the specimen to specimen variation in the microstructure. The microstructure of three RD bend specimens are shown in Fig. 13(a)-(c) together with the zoomed view of the local microstructure in the center of the bend specimen and the crack nucleation site. The volume fraction of the ferrite phase in the local microstructure at the center of the bend specimens shown in Fig. 13(a)–(c) are ≈ 0.66, ≈ 0.44 and ≈ 0.29, respectively, while the volume fraction of the ferrite phase in the local microstructure at the first crack nucleation sites are ≈ 0.52, ≈ 0.58 and ≈ 0.49, respectively. This suggests that a right combination of the amount of ferrite phase and constraint imposed by the martensite phase is needed to nucleate a crack. Anyhow, our analyses show that the values of ε_f can be correlated with the projected distance between the center of the bend specimens and the crack nucleation site. As shown in Fig. 13(d), the value of ε_f increases with increasing distance between the center of the bend specimen and the crack nucleation site.

The microstructure-based finite element calculations here have been carried out using a fixed finite element mesh so the question arises as to the extent of mesh dependence. In a grid based calculation such as finite element method, in the absence of a physical length-scale, the finite element mesh size is the dominant length-scale. However, in the microstructure-based finite element calculations, the discretely modeled material microstructure introduces microstructural length-scale(s). This is apparent from the predicted difference in the ductile fracture response of RD and TD specimens of DP steel sheets under bending. In addition, the rate dependence in the constitutive relation, Eq. (7), also regularizes the mesh dependence issues associated with localization of deformation (Needleman, 1988). Although, it is not possible to guarantee that the finite element mesh size does not play any role, our simple mesh convergence study show that for the mesh size considered here, the role of mesh size is not dominant. Here, we assess the finite element mesh size convergence by carrying out bending calculations of a RD specimen with element sizes, $e = 8.3\mu m$, $10.0\mu m$, and $12.5\mu m$ in the fine mesh region (marked as *abcd* in Fig. 1) and comparing the predicted values of ε_f. The results of this exercise show that decreasing the mesh size from $12.5\mu m$ to $10.0\mu m$ results in a $\approx 8.6\%$ decrease in the value of ε_f, whereas further decreasing the mesh size from $10.0\mu m$ to $8.3\mu m$ results in an insignificant change in the value of ε_f.

5. Concluding remarks

We have carried out microstructure-based finite element modeling to understand the influence of the interlacing of length-scales induced by 90° V-bend loading conditions and microstructure on ductile crack nucleation and early stage ductile crack growth in a DP steel with tensile strength of order 1*GPa*. In the calculations, the microstructural features, ferrite and martensite phases, of the DP steel are discretely modeled in a thin slice of bend specimen normal to the bend axis using a constitutive relation for progressively cavitating elastic-viscoplastic solid. The calculations are carried out for several microstructures taken from both RD and TD cross-sections of the DP steel sheet. Parametric studies are also carried out to explore the effect of material parameters that govern the ductile damage and crack nucleation.

The key conclusions are as follows:

1. In-line with the experimental observations, our calculations predict that despite similar strength and strain hardenability, volume fraction of the phases, and fracture response under uniaxial tension along RD and TD, the bendability of RD specimens are less than the bendability of TD specimens. The difference between the bendability of RD and TD specimens in our calculations naturally emerge due to the differences in the topological features of the microstructure along RD and TD.
2. The interlacing of length-scales induced by bending and DP microstructure results in an overall gradient in the distribution of equivalent plastic strain, $\bar{\varepsilon}$, with the value of $\bar{\varepsilon}$ being greater at the surface and within this gradient the value of $\bar{\varepsilon}$ being greater in the ferrite phase close to the ferrite-martensite interface.
3. The greater values of $\bar{\varepsilon}$ in the ferrite phase close to the ferrite-martensite interface results in void nucleation at these locations. The growth of these nucleated voids, however, depends on the constrained imposed by the local distribution of the martensite phase.
4. A variation in the values of the material parameters that govern the ductile damage and crack nucleation in the ferrite phase significantly affect the bendability of DP steel sheets. Thus, efforts to improve the bendability of DP steel sheets must focus on improving the mechanical properties of the ferrite phase.
5. The variation in the bendability of DP steel sheet specimens with fixed overall microstructure and sheet orientation can be correlated with the distance between the center of the bend specimen and the crack nucleation site, such that an increase in the distance results in an increase in the bendability.

Acknowledgments

The large-scale finite element calculations reported on were carried out using high performance research computing resources provided by Texas A&M University (http://hprc.tamu.edu). The financial support provided by the ArcelorMittal Global R&D, East Chicago, IN, USA, and U.S. National Science Foundation grant CMMI - 1663130 are gratefully acknowledged. The authors are very grateful for the many fruitful discussions with Pallava Kaushik, Gang Huang and other engineers of the ArcelorMittal Global R&D, East Chicago, IN, USA.

References

Alaie, A., Kadkhodapour, J., Rad, S.Z., Asadabad, M.A., Schmauder, S., 2015. Formation and coalescence of strain localized regions in ferrite phase of dp600 steels under uniaxial tensile deformation. Mater. Sci. Eng. A 623, 133–144.
Andrade, F., Feucht, M., Haufe, A., Neukamm, F., 2016. An incremental stress state dependent damage model for ductile failure prediction. Int. J. Fract. 200 (1–2), 127–150.
Avramovic-Cingara, G., Ososkov, Y., Jain, M., Wilkinson, D., 2009. Effect of martensite distribution on damage behaviour in dp600 dual phase steels. Mater. Sci. Eng. A 516 (1–2), 7–16.
Avramovic-Cingara, G., Saleh, C.A., Jain, M., Wilkinson, D., 2009. Void nucleation and growth in dual-phase steel 600 during uniaxial tensile testing. Metall. Mater. Trans. A 40 (13), 3117.
Ayatollahi, M., Darabi, A.C., Chamani, H., Kadkhodapour, J., 2016. 3d micromechanical modeling of failure and damage evolution in dual phase steel based on a real 2d microstructure. Acta Mech. Solida Sin. 29 (1), 95–110.
Bao, Y., Wierzbicki, T., 2004. On fracture locus in the equivalent strain and stress triaxiality space. Int. J. Mech. Sci. 46 (1), 81–98.
Belytschko, T., Chiapetta, R.L., Bartel, H.D., 1976. Efficient large scale non-linear transient analysis by finite elements. Int. J. Numer. Methods Eng. 10 (3), 579–596.
Benzerga, A.A., Leblond, J.-B., Needleman, A., Tvergaard, V., 2016. Ductile failure modeling. Int. J. Fract. 201 (1), 29–80.
Bhattacharya, D., 2011. Metallurgical perspectives on advanced sheet steels for automotive applications. In: Advanced Steels. Springer, pp. 163–175.
Chen, P., Ghassemi-Armaki, H., Kumar, S., Bower, A., Bhat, S., Sadagopan, S., 2014. Microscale-calibrated modeling of the deformation response of dual-phase steels. Acta Mater. 65, 133–149.
Choi, K.S., Liu, W.N., Sun, X., Khaleel, M.A., 2009. Influence of martensite mechanical properties on failure mode and ductility of dual-phase steels. Metall. Mater. Trans. A 40 (4), 796–809.
Choi, S.-H., Kim, E.-Y., Woo, W., Han, S., Kwak, J., 2013. The effect of crystallographic orientation on the micromechanical deformation and failure behaviors of dp980 steel during uniaxial tension. Int. J. Plast. 45, 85–102.
Chu, C., Needleman, A., 1980. Void nucleation effects in biaxially stretched sheets. J. Eng. Mater. Technol. 102 (3), 249–256.
Davies, R., 1978. Influence of martensite composition and content on the properties of dual phase steels. Metall. Trans. A 9 (5), 671–679.
De Geus, T., Peerlings, R., Geers, M., 2015. Microstructural topology effects on the onset of ductile failure in multi-phase materials–a systematic computational approach. Int. J. Solids Struct. 67, 326–339.
De Geus, T., Peerlings, R., Geers, M., 2017. Fracture in multi-phase materials: why some microstructures are more critical than others. Eng. Fract. Mech. 169, 354–370.
De Geus, T., van Duuren, J., Peerlings, R., Geers, M., 2016. Fracture initiation in multi-phase materials: a statistical characterization of microstructural damage sites. Mater. Sci. Eng. A 673, 551–556.
Embury, J.D., Duncan, J.L., Mar 1982. Formability of dual-phase steels. J. Occup. Med. 34 (3), 24–29.
Gerbig, D., Srivastava, A., Osovski, S., Hector, L.G., Bower, A., 2018. Analysis and design of dual-phase steel microstructure for enhanced ductile fracture resistance. Int. J. Fract. 209 (1–2), 3–26.

Ghoreishi, S.F., Molkeri, A., Srivastava, A., Arroyave, R., Allaire, D., 2018. Multi-information source fusion and optimization to realize icme: application to dual-phase materials. J. Mech. Des. 140 (11), 111409.
Gurson, A.L., 1975. Plastic Flow and Fracture Behavior of Ductile Materials Incorporating Void Nucleation, Growth and Coalescence. PhD Diss. Brown University.
Hasegawa, K., Kawamura, K., Urabe, T., Hosoya, Y., 2004. Effects of microstructure on stretch-flange-formability of 980 mpa grade cold-rolled ultra high strength steel sheets. ISIJ Int. 44 (3), 603–609.
Huang, S., He, C., Zhao, Y., 2016. Microstructure-based rve approach for stretch-bending of dual-phase steels. J. Mater. Eng. Perform. 25 (3), 966–976.
Joost, W.J., 2012. Reducing vehicle weight and improving us energy efficiency using integrated computational materials engineering. JOM (J. Occup. Med.) 64 (9), 1032–1038.
Kadkhodapour, J., Butz, A., Ziaei-Rad, S., Schmauder, S., 2011. A micro mechanical study on failure initiation of dual phase steels under tension using single crystal plasticity model. Int. J. Plast. 27 (7), 1103–1125.
Kuziak, R., Kawalla, R., Waengler, S., 2008. Advanced high strength steels for automotive industry. Arch. Civ. Mech. Eng. 8 (2), 103–117.
Lai, Q., Bouaziz, O., Gouné, M., Brassart, L., Verdier, M., Parry, G., Perlade, A., Bréchet, Y., Pardoen, T., 2015. Damage and fracture of dual-phase steels: influence of martensite volume fraction. Mater. Sci. Eng. A 646, 322–331.
Lai, Q., Brassart, L., Bouaziz, O., Gouné, M., Verdier, M., Parry, G., Perlade, A., Bréchet, Y., Pardoen, T., 2016. Influence of martensite volume fraction and hardness on the plastic behavior of dual-phase steels: experiments and micromechanical modeling. Int. J. Plast. 80, 187–203.
Leu, D.-K., 1997. A simplified approach for evaluating bendability and springback in plastic bending of anisotropic sheet metals. J. Mater. Process. Technol. 66 (1–3), 9–17.
Liu, Y., Zheng, X., Osovski, S., Srivastava, A., 2019. On the micromechanism of inclusion driven ductile fracture and its implications on fracture toughness. J. Mech. Phys. Solids 130, 21–34.
Luo, M., Wierzbicki, T., 2010. Numerical failure analysis of a stretch-bending test on dual-phase steel sheets using a phenomenological fracture model. Int. J. Solids Struct. 47 (22–23), 3084–3102.
Marcadet, S.J., Mohr, D., 2015. Effect of compression–tension loading reversal on the strain to fracture of dual phase steel sheets. Int. J. Plast. 72, 21–43.
MATLAB, R, 2017. Image Processing Toolbox. The MathWorks Inc., Natick, MA, USA.
Matsuno, T., Teodosiu, C., Maeda, D., Uenishi, A., 2015. Mesoscale simulation of the early evolution of ductile fracture in dual-phase steels. Int. J. Plast. 74, 17–34.
Needleman, A., 1988. Material rate dependence and mesh sensitivity in localization problems. Comput. Methods Appl. Mech. Eng. 67 (1), 69–85.
Nsouglo, K.E., Srivastava, A., Osovski, S., Rodríguez-Martínez, J.A., 2018. Random distributions of initial porosity trigger regular necking patterns at high strain rates. Proc. R. Soc. A Math. Phys. Eng. Sci. 474 (2211), 20170575.
Osovski, S., Srivastava, A., Ponson, L., Bouchaud, E., Tvergaard, V., Ravi-Chandar, K., Needleman, A., 2015. The effect of loading rate on ductile fracture toughness and fracture surface roughness. J. Mech. Phys. Solids 76, 20–46.
Osovski, S., Srivastava, A., Williams, J.C., Needleman, A., 2015. Grain boundary crack growth in metastable titanium β alloys. Acta Mater. 82, 167–178.
Pan, J., Saje, M., Needleman, A., 1983. Localization of deformation in rate sensitive porous plastic solids. Int. J. Fract. 21 (4), 261–278.
Paul, S.K., 2012. Micromechanics based modeling of dual phase steels: prediction of ductility and failure modes. Comput. Mater. Sci. 56, 34–42.
Peirce, D., Shih, C.F., Needleman, A., 1984. A tangent modulus method for rate dependent solids. Comput. Struct. 18 (5), 875–887.
Perzyński, K., Madej, Ł., Wang, J., Kuziak, R., Hodgson, P.D., 2014. Numerical investigation of influence of the martensite volume fraction on dp steels fracture behavior on the basis of digital material representation model. Metall. Mater. Trans. A 45 (13), 5852–5865.
Pineau, A., Benzerga, A.A., Pardoen, T., 2016. Failure of metals i: brittle and ductile fracture. Acta Mater. 107, 424–483.
Ramos, L.F., Matlock, D.K., Krauss, G., 1979. On the deformation behavior of dual-phase steels. Metall. Mater. Trans. A 10 (2), 259–261.
Rashid, M.S., 1981. Dual phase steels. Annu. Rev. Mater. Sci. 11 (1), 245–266.
Roth, C.C., Mohr, D., 2014. Effect of strain rate on ductile fracture initiation in advanced high strength steel sheets: experiments and modeling. Int. J. Plast. 56, 19–44.
Sodjit, S., Uthaisangsuk, V., 2012. Microstructure based prediction of strain hardening behavior of dual phase steels. Mater. Des. 41, 370–379.
Sriram, S., Wong, C., Huang, M., Yan, B., 2003. Stretch bendability of advanced high strength steels (SAE Transactions No. 2003-01-1151). Journal of Materials and Manufacturing 112, 641–649.
Srivastava, A., Bower, A., Hector Jr., L., Carsley, J., Zhang, L., Abu-Farha, F., 2016. A multiscale approach to modeling formability of dual-phase steels. Model. Simul. Mater. Sci. Eng. 24 (2), 025011.
Srivastava, A., Ghassemi-Armaki, H., Sung, H., Chen, P., Kumar, S., Bower, A.F., 2015. Micromechanics of plastic deformation and phase transformation in a three-phase trip-assisted advanced high strength steel: experiments and modeling. J. Mech. Phys. Solids 78, 46–69.
Srivastava, A., Osovski, S., Needleman, A., 2017. Engineering the crack path by controlling the microstructure. J. Mech. Phys. Solids 100, 1–20.
Srivastava, A., Ponson, L., Osovski, S., Bouchaud, E., Tvergaard, V., Needleman, A., 2014. Effect of inclusion density on ductile fracture toughness and roughness. J. Mech. Phys. Solids 63, 62–79.
Steinbrunner, D.L., Matlock, D., Krauss, G., 1988. Void formation during tensile testing of dual phase steels. Metall. Trans. A 19 (3), 579–589.
Sun, X., Choi, K.S., Liu, W.N., Khaleel, M.A., 2009. Predicting failure modes and ductility of dual phase steels using plastic strain localization. Int. J. Plast. 25 (10), 1888–1909.
Sun, X., Choi, K.S., Soulami, A., Liu, W.N., Khaleel, M.A., 2009. On key factors influencing ductile fractures of dual phase (dp) steels. Mater. Sci. Eng. A 526 (1–2), 140–149.
Tasan, C.C., Diehl, M., Yan, D., Bechtold, M., Roters, F., Schemmann, L., Zheng, C., Peranio, N., Ponge, D., Koyama, M., et al., 2015. An overview of dual-phase steels: advances in microstructure-oriented processing and micromechanically guided design. Annu. Rev. Mater. Res. 45, 391–431.
Tasan, C.C., Hoefnagels, J.P., Diehl, M., Yan, D., Roters, F., Raabe, D., 2014. Strain localization and damage in dual phase steels investigated by coupled in-situ deformation experiments and crystal plasticity simulations. Int. J. Plast. 63, 198–210.
Tvergaard, V., 1981. Influence of voids on shear band instabilities under plane strain conditions. Int. J. Fract. 17 (4), 389–407.
Tvergaard, V., 1982. Influence of void nucleation on ductile shear fracture at a free surface. J. Mech. Phys. Solids 30 (6), 399–425.
Tvergaard, V., 1982. On localization in ductile materials containing spherical voids. Int. J. Fract. 18 (4), 237–252.
Tvergaard, V., Needleman, A., 1984. Analysis of the cup-cone fracture in a round tensile bar. Acta Metall. 32 (1), 157–169.
Uthaisangsuk, V., Prahl, U., Bleck, W., 2009. Characterisation of formability behaviour of multiphase steels by micromechanical modelling. Int. J. Fract. 157 (1–2), 55.
Uthaisangsuk, V., Prahl, U., Bleck, W., 2009. Failure modeling of multiphase steels using representative volume elements based on real microstructures. Procedia Eng. 1 (1), 171–176.
Uthaisangsuk, V., Prahl, U., Bleck, W., 2011. Modelling of damage and failure in multiphase high strength dp and trip steels. Eng. Fract. Mech. 78 (3), 469–486.
Vajragupta, N., Uthaisangsuk, V., Schmaling, B., Münstermann, S., Hartmaier, A., Bleck, W., 2012. A micromechanical damage simulation of dual phase steels using xfem. Comput. Mater. Sci. 54, 271–279.
Yerra, S., Martin, G., Veron, M., Brechet, Y., Mithieux, J., Delannay, L., Pardoen, T., 2013. Ductile fracture initiated by interface nucleation in two-phase elastoplastic systems. Eng. Fract. Mech. 102, 77–100.
Zhou, J., Gokhale, A.M., Gurumurthy, A., Bhat, S.P., 2015. Realistic microstructural rve-based simulations of stress–strain behavior of a dual-phase steel having high martensite volume fraction. Mater. Sci. Eng. A 630, 107–115.